



ELSEVIER

Contents lists available at ScienceDirect

Acta Materialia

journal homepage: www.elsevier.com/locate/actamat

Research paper

Oxygen injection during fast vs slow passivation in aqueous solution

Xiao-Xiang Yu^{a,*}, Junsoo Han^b, John R. Scully^b, Laurence D. Marks^a^a Department of Materials Science and Engineering, Northwestern University, Evanston, IL, 60208, USA^b Department of Materials Science and Engineering, University of Virginia, Charlottesville, VA, 22904, USA

ARTICLE INFO

Article history:

Received 28 November 2020

Revised 1 April 2021

Accepted 11 April 2021

Available online 24 April 2021

Keywords:

Corrosion

Transmission electron microscopy

Molybdenum

Nickel-based alloys

ABSTRACT

The typical defect reactions at the metal/oxide interface, which explain the growth and breakdown of passive oxide films in corrosion, include creating metal and oxygen vacancies. While the creation and coalescence of metal vacancies are well documented, there are relatively few observations on the nanoscale details of oxygen transport near the metal/oxide interface. We report here a new mechanism of oxygen injection into the metal. Fast and slow passivation (i.e., corrosion involving both oxide film growth and direct dissolution) of NiCr and NiCrMo alloys was performed by galvanostat experiments in 0.1 M NaCl (pH 4) deaerated solution. Localized regions of an unexpected nonequilibrium metal-based oxygen solid solution were observed beneath the outer (externally formed) oxides, and the saturated oxygen atoms distorted the fcc metallic lattices. Oxygen injection into the metal is more significant at a fast growth rate due to a large passivation current density for the NiCr alloy. In this case, there is a high volume of rock salt Ni(Cr)O nanocrystals in the O-rich Ni(Cr) substrate, which is consistent with greater susceptibility to chloride-induced breakdown found in potentiostat experiments. The addition of Mo promotes the formation of the corundum phase in the outer oxide layer for NiCrMo, which changes the transport mechanism as well as the diffusivity of oxygen through the oxide film and across the metal/oxide interface.

© 2021 Acta Materialia Inc. Published by Elsevier Ltd. All rights reserved.

1. Introduction

Passivity of metallic materials is critical to our metals-based civilization [1]. Many metals and alloys exhibit extraordinary kinetic stability in oxidizing environments due to the existence of thin oxide films on metal (or alloy) surfaces. This passivating oxide film prevents the metal from attack by the corrosive environment so long as it remains intact and does not break down. A critical issue in both gaseous oxidation and aqueous corrosion is understanding under what conditions breakdown is prevalent and why it occurs.

Numerous models have been proposed to account for the kinetics of passive oxide formation, growth, and breakdown [2–18]; we will provide a brief background here. All these models describe the system via a combination of point defects in the oxide and electrostatic terms. The solubility of oxygen in the metals of interest is small, and the metal is assumed to at most include some vacancies [19,20]. We will use here the Point Defect Model (PDM) [15–18,21] as a basis. In the PDM, typical defect reactions include at the metal/oxide interface: (1) oxidation of metal and creation of metal

vacancies; (2) generation of cation interstitials in the oxide; (3) creation of anion (oxygen) vacancies. At the external oxide/ambient environment interface, similar processes take place due to oxide growth or dissolution: (1) generation of cation vacancies and annihilation of cation interstitials; (2) annihilation of anion vacancies; (3) dissolution of the barrier layer.

These different processes are coupled to transport equations in the oxide combining chemical potential gradient and electrostatic contributions, implicitly assuming local equilibrium (reversible thermodynamics) at the interfaces. Normally the models are reduced to one dimension, in effect considering some mean-field average over microstructure, composition, and crystallography, which may be a severe approximation [22].

One common approach to breakdown is to consider it as a consequence of large numbers of cation vacancies coalescing at the oxide/metal interface as well as Kirkendall voids due to differences in Ni and Cr transport rates, for which there is extensive experimental and computational evidence in both oxide and metal [23–29]. If these occur at the metal/oxide interface, they can lead to rupture or delamination, exposing the underlying metal to attack. While there is certainly good evidence that this can occur, it does not need to be the only mechanism for failure – different conditions may well lead to different breakdown processes [30]. Usually, the metal itself is not considered as a significant player in breakdown

* Corresponding author.

E-mail addresses: yuxx07@gmail.com, xiaoxiang.yu@northwestern.edu (X.-X. Yu).

processes, except perhaps via these Kirkendall voids; as we will see, this is not always correct.

Beyond this general corrosion theory, various models have also been developed to predict specific alloys' passivity. In particular, minor alloying elements such as molybdenum (Mo) have experimentally significant effects on the localized corrosion resistance of many alloys [31–34]. Earlier explanations of the role of Mo fall into three broad categories: (1) Mo could stabilize cation vacancies minimizing the formation of voids [35]; (2) passivation due to a critical concentration of Cr plus minor amounts of Mo at active localized corrosion sites [36,37], focusing on compositional, electronic, and physical features of the oxide such as the film thickness and microstructure of passivating layers [33,38]; (3) a role for Mo in the latter stage of corrosion, such as at crevice sites promoting repassivation [39,40].

It has recently become clear that some of the assumptions in these approaches are open to question and may be invalid. First, when the velocity of metal/oxide moving interface is faster than solute atom interfacial diffusivity, local equilibrium at the metal/oxide interface is often violated, leading to nonequilibrium solute capture [41,42]. In this case, the cation composition of the resulting oxide can be far from what one would otherwise expect [43]. For instance, one can easily have a rock salt $\text{Ni}_{1-x}\text{Cr}_{2x/3}\text{O}$ where the fraction x significantly exceeds the thermodynamical solubility limit. For completeness, we are using the term “rock salt” here (later) and “corundum” following standard crystallographic convention where these are structure types, not specific compositions; see [41,42], for further discussion. Second, both theoretically [14] and experimentally [44,45], there can be morphological instabilities leading to non-planar interfaces – using a perfectly planar and thus 1-D high field model assumption can be misleading as it omits essential phenomena. Third, as we have recently discussed [46], crystallographic variations can be significant, so mean-field averages are open to question. Last, there is growing evidence on oxide phase changes. For instance, Mo promotes a corundum phase with some additional nonequilibrium solute captured species [47,48].

Do we yet have a complete model, or are there other assumptions in the literature that should be questioned? As mentioned above, the solubility of oxygen in the transition metal such as Ni is typically low, particularly for the temperature of most aqueous corrosion cases. In other metals such as Zr, Ta, and Nb, where oxides grow by anion ingress, the oxygen flux arriving at the metal/oxide interface is large. Oxygen may react with metal or enter the metal in solid solution [27]. The equilibrium oxygen solubility in these metals (e.g., Zr [49], Ta [50], Nb [51]) is large and increases with temperature. Oxygen in solid solution is often seen under externally oxidized test samples. In contrast, oxygen solubility is low [52], and high oxygen content above equilibrium solubility has not been reported in transition metals, especially near room temperature during aqueous corrosion. However, ignoring oxygen injection into a transition metal with lower O solubility is only valid if there is local equilibrium at the metal/oxide interface. If there is not, the oxygen chemical potential could be high enough to force oxygen dissolution into the metal. As we will demonstrate here this is, in fact, the case for rapid passivation.

Specifically, in this study fast and slow aqueous repassivation of NiCr and NiCrMo alloys was performed by galvanostat experiments in 0.1 M NaCl (pH 4) deaerated solution. Regions of localized oxygen injection in the underlying alloy were found throughout TEM cross-section samples beneath the outer oxide layer, where the saturated oxygen atoms distorted the fcc metallic lattices. Oxygen injection into the metal is more significant during fast growth with a large passivation current density applied to NiCr. Moreover, a high volume of the rock salt oxide phase is mixed with the O-rich metal substrate. High oxygen dissolution conditions in the al-

loy are associated with stabilizing cation vacancies near the interface due to available electrons in the metal. Mo promotes the formation of the corundum phase in the outer oxide layer for NiCrMo, which changes the transport mechanism and the diffusivity of oxygen through the oxide film and across the metal/oxide interface.

2. Experimental and computational methods

Ni-22%Cr and Ni-22%Cr-6%Mo (wt.%) alloys were prepared from pure components (>99.99%) by arc melting. The samples were then homogenized in a tube furnace at 1000°C for 5 hours followed by a water quench. All samples were ground to 4000 grit using SiC paper under deionized (DI) water, 18 M Ω cm obtained via a Millipore system, then finished with polycrystalline diamond suspension to 0.25 μm . Samples were rinsed with DI water, then dried with flowing N_2 gas.

All the electrochemical experiments were performed in the 0.1 M NaCl solution with a final pH adjusted to 4.0 using 1.0 M HCl. The solution was deaerated by N_2 gas during the measurement to maintain the oxygen concentration at a low level and the same in the electrolyte for each experiment. A Gamry Reference 600™ potentiostat was used to control and measure the electrochemical current and potential. A standard three-electrode electrochemical cell was used with a saturated calomel electrode (SCE) as a reference electrode and a Pt mesh as a counter electrode (CE). The sample surface was exposed to the electrolyte with a surface area defined as 0.1 cm^2 from an O-ring, inert to the chemical reaction. Prior to the galvanostatic experiments, a constant potential at -1.3 V vs. SCE was applied for 600 s to minimize the air-formed oxide. Either fast or slow galvanostatic passivation experiments were performed. Specifically, a constant current of 50 $\mu\text{A cm}^{-2}$ (fast) or 0.5 $\mu\text{A cm}^{-2}$ (slow) was applied while the potential was recorded as a function of time until the potential reached +200 mV vs. SCE, just below the onset potential of metastable pitting. It should be recognized that at 0.5 $\mu\text{A cm}^{-2}$ the applied anodic current density likely underestimates the true anodic current density due to residual oxygen reduction. After each experiment, the sample surface was characterized by a microscope, and no crevice corrosion was seen except in the Ni-Cr alloy case during slow growth. Another set of galvanostatically passivated samples were immediately subjected to a constant potential at $E_{\text{ap}} = +200$ mV vs. SCE for 10,000 s to monitor the passive film's stability and metastable pitting events indicated by current bursts in current density vs. time data.

The electrochemically tested samples were immediately sealed in a portable vacuum chamber (Vacu-Storr™) provided by Ted Pella, Inc. for the TEM characterization. Samples for electron microscopy were prepared and analyzed within three months; however, we believe the relaxation of the passivated oxide layer and the oxidation-influenced region would be negligible at room temperature and under low oxygen pressure. TEM samples were lifted out after the deposition of Pt protective layers on the passivated surface in the FEI Helios Nanolab focused ion beam instrument and then thinned using beam energy of 30 kV. Low energy (2 kV) final cleaning was used to reduce the amorphous layer thickness. Atomic resolution scanning transmission electron microscopy (STEM) imaging was acquired using an aberration-corrected JEOL ARM200CF microscope. Collection angle β was $11 \text{ mrad} \leq \beta \leq 22 \text{ mrad}$ for the annular bright field (ABF) imaging and $90 \text{ mrad} \leq \beta \leq 220 \text{ mrad}$ for the high angle annular dark field (ADF) imaging. ADF and ABF images were taken simultaneously. Compositional analysis was performed using energy-dispersive x-ray spectroscopy (EDS) with a dual silicon drift detector.

To elucidate the role of cation vacancies coupled with the interstitial oxygen in the metal, spin-polarized density functional theory (DFT) calculations were performed using the Vienna *Ab initio*

Simulation Package (VASP) [53–55] with the projector augmented wave method [56]. Calculating the energetics of a system such as a Ni/NiO interface using density functional theory involves making significant approximations. Unfortunately, while standard functionals do a decent job for metals such as fcc Ni, they do not for strongly correlated oxides such as NiO. We therefore compromised, using the SCAN meta-GGA [57,58] in all the simulations, leading to reasonable values for the lattice parameters and formation energies but too small values for the band gap and magnetic moment. Hence, the results are semiquantitative only. 550 eV was chosen for the plane wave cutoff, and the k points sampling used the Monkhorst–Pack scheme [59]. The electronic structures were relaxed with a convergence of 10^{-5} eV for the total energy, and the atomic structures were relaxed until the forces on each ion were less than 0.01 eV/Å.

3. Results

We will first describe the electrochemical results before turning to the structural analysis, which provides critical information on what is taking place; an explanation will be provided in the discussion.

3.1. Electrochemical passivation of NiCr and NiCrMo alloys under fast and slow galvanostatic growth

Upon application of a high anodic galvanostatic current density (i.e., 50 $\mu\text{A}/\text{cm}^2$) to the Ni-22Cr alloy, the applied potential vs. the SCE reference electrode increases almost linearly with the time of application except for initial stripping by oxidation of any hydrogen generated which takes about 10 seconds (Fig. 1(a)). This hydrogen is produced due to the initial cathodic reduction step as discussed above, where adsorbed hydrogen is deposited and then oxidized. The potential of +0.2 V vs. SCE is reached in about 70 seconds after about 3.5 mC/cm^2 of anodic charge density is passed (stars). Similar behavior is seen in the case of NiCrMo with little difference between Ni-22Cr and Ni-22Cr-6Mo. A positive linear increase in potential, $E(t)$, versus growth time indicates passivation during the galvanostatic growth. The oxide thickens roughly linearly with time with $E(t)$, and the voltage gradient across the oxide is thus relatively constant during galvanostatic growth. The potential drop across the interface also likely rises to control and sustain a fixed reaction rate. To do this, the potential, E , must be driven linearly to higher values as observed. The increase in E is indicative of this condition and is entirely consistent with the Cabrera-Mott [3–5], Point Defect Model [15–18,21], or Generalized Growth Passivation Models [9,10].

Moreover, the slope E - t changes slightly with time and potential, indicating the evolution of oxide characteristics as both its composition and thickness change over time. In general, a high slope or fast potential rise indicates efficient passivation and facile growth. When the potential is constant with time and does not rise, there is a finite anodic current density indicative of a resistive interface undergoing oxidation and possibly cation ejection into solution instead of oxide growth, as shown by Ogle and collaborators [60]. In that case, the surface is poorly passivated, and some cation ejection occurs instead of film growth and thickening. These cations have been measured by AESEC [61]. In fact, a significant breakdown would produce no rise in $E(t)$. In Fig. 1(b), it can be seen that the time to reach +0.2 V vs. SCE is slower as expected when 0.5 $\mu\text{A}/\text{cm}^2$ is applied (about 9000 sec for Ni-Cr-Mo or 4.5 mC/cm^2) and, secondly, never reaches +200 mV during the experiment in the NiCr alloy without Mo indicative of the possible breakdown effects described above. Indeed, the potential does not fully attain +0.2 V vs. SCE in 10,000 s for the NiCr alloy, while the NiCrMo alloy is passivated to this potential in 9000 sec

after 4.5 mC/cm^2 (star). Finally, it should be noted that even for NiCrMo, the conversion efficiency of oxidized Ni and Cr found in the oxide (or hydroxide) as opposed to directly ejected in solution or oxide dissolution is often less than 100% [62]. This is particularly true in acidic solutions when oxides may be metastable. The consequence of this would be that the flux of cation (metal) vacancies injected into the substrate is slightly larger than just the number of moles of oxidized metal found in the oxide. 3.5 to 4.5 mC/cm^2 of anodic charge is passed, as is evident from the data during both slow and fast growth. The charge may be slightly higher at the low rate as the applied current density is less than the true anodic current density due to residual oxygen reduction on the electrode even after deaeration. 1 nm of ideal compact rocksalt oxide with no porosity requires about 1.5–2 mC/cm^2 of charge, neglecting finite values of x in $\text{Ni}_{1-x}\text{Cr}_x\text{O}$. Porous outer hydroxides may produce 1 nm per mC/cm^2 of more voluminous films due to lower hydroxide density. Thus, oxide thicknesses from 3.5–4.5 nm might be expected from these electrochemical assessments, but a better definition is obtained from TEM cross-sections below. Less than 100% efficiency would lead to a situation where the total anodic charge devoted to the oxide is slightly less than the total anodic charge, as is discussed elsewhere [61].

3.2. Passive film growth and breakdown during 10,000 s potential holds

After fast or slow oxide formation and growth, the alloys were held at a nominally passive potential for 10,000 s to investigate which condition was more resistant to corrosion in 0.1 M NaCl acidified to pH 4. The potentiostatic hold enables passivation and possible breakdown of the passive film already formed by fast or slow growth. Three general features are observed during the subsequent potential hold for 10,000 s at +0.2 V vs. SCE. These are (1) gradual current density decay due to additional passivation and/or beneficial exposure aging, (2) gradual current density decay followed by an abrupt rise signaling initial film growth followed by breakdown, respectively, or (3) a high steady anodic current density indicating that the alloy underwent breakdown during the galvanostatic phase. The first (1) can be attributed to oxide film thickening, which at constant potential may result in a lowering of the voltage gradient across the oxide and likely alters the potential drop at the metal/oxide and oxide/electrolyte interfaces as well, while (2) indicates abrupt breakdown during passivation or (3) sustained breakdown. In general, current densities are higher after fast growth compared to slow growth for each alloy (Fig. 1(c) and (d)). The current density in the former case decays for NiCr, and then breakdown occurs instantaneously at about 500 s (Fig. 1(c)). In contrast, the current density on the NiCrMo alloys decays steadily (Fig. 1(c)). In the case of slow growth, the current density is lower for the NiCrMo alloy. It decays indicative of passive film thickening while the current on the NiCr alloy is high the entire 10,000 s suggesting small areas of breakdown, which is on-going (Fig. 1(d)).

3.3. Passivation and microstructural analysis

The fast-growth passivating oxide thin film on the Ni-22Cr sample was examined by TEM using cross-sectional samples, as shown in Fig. 2(a) from the region labeled in Fig. 2(d) at a lower magnification. The outermost layer is a rock salt oxide similar to NiO, but with partial substitution of Cr for Ni due to nonequilibrium solute capture [41,45,47]. There is about 20 nm thick rock salt and fcc Ni(Cr) nanocrystalline mixture layer beneath, as indicated in the power spectrum in Fig. 2(c). Fourier filtering of the images in Fig. 2(b) highlights the rock salt nanoparticles formed both within the mixture layer and at the oxide/metal interface, indicating the

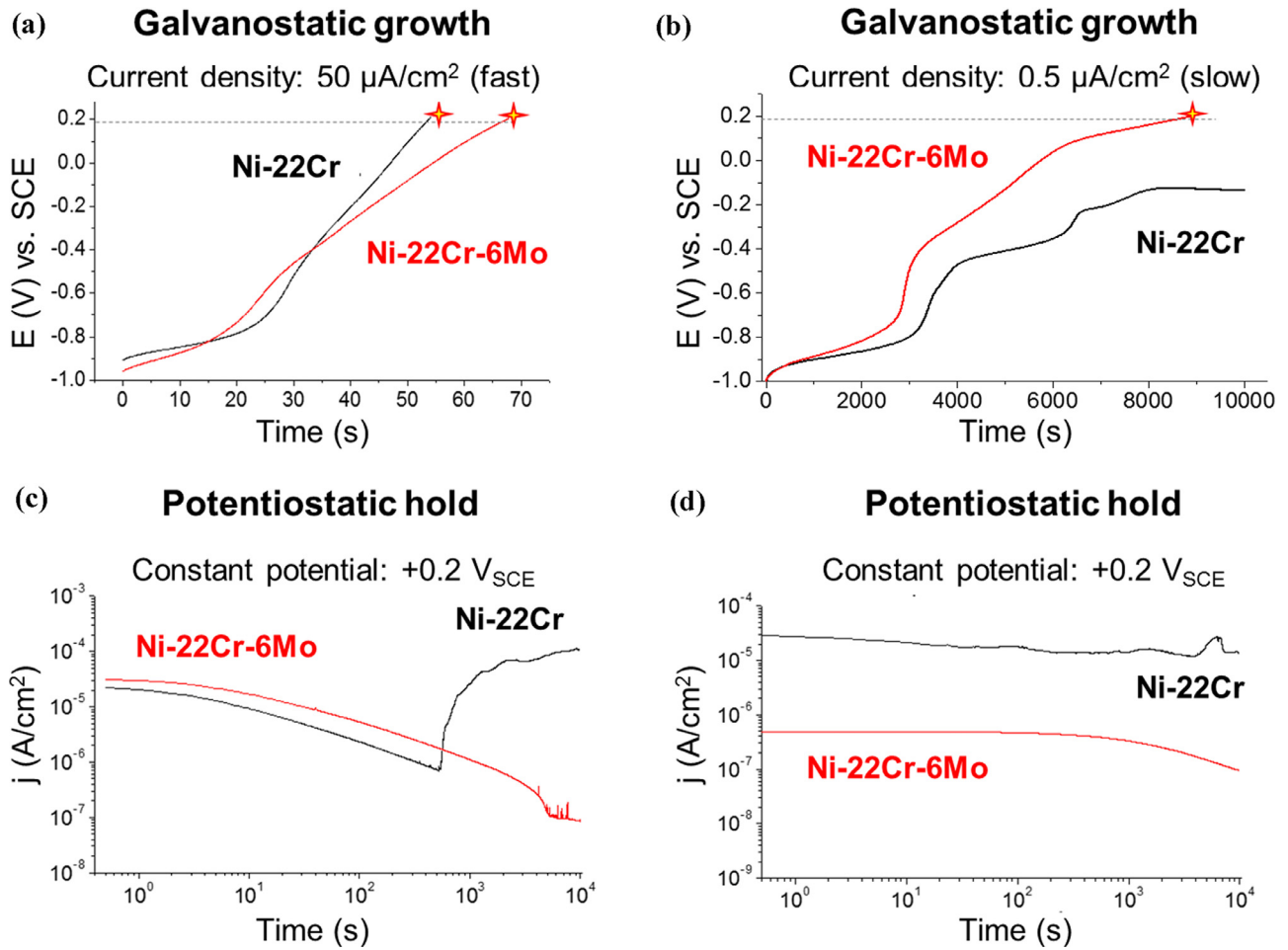


Fig. 1. The potential E vs. an SCE reference electrode as a function of time for the electrochemical passivation of NiCr and NiCrMo alloys in 0.1 M NaCl (pH 4) under (a) fast and (b) slow galvanostatic growth conditions. Potentiostatic hold for 10,000 seconds at +0.2 V vs. SCE after (c) fast and (d) slow galvanostatic growth.

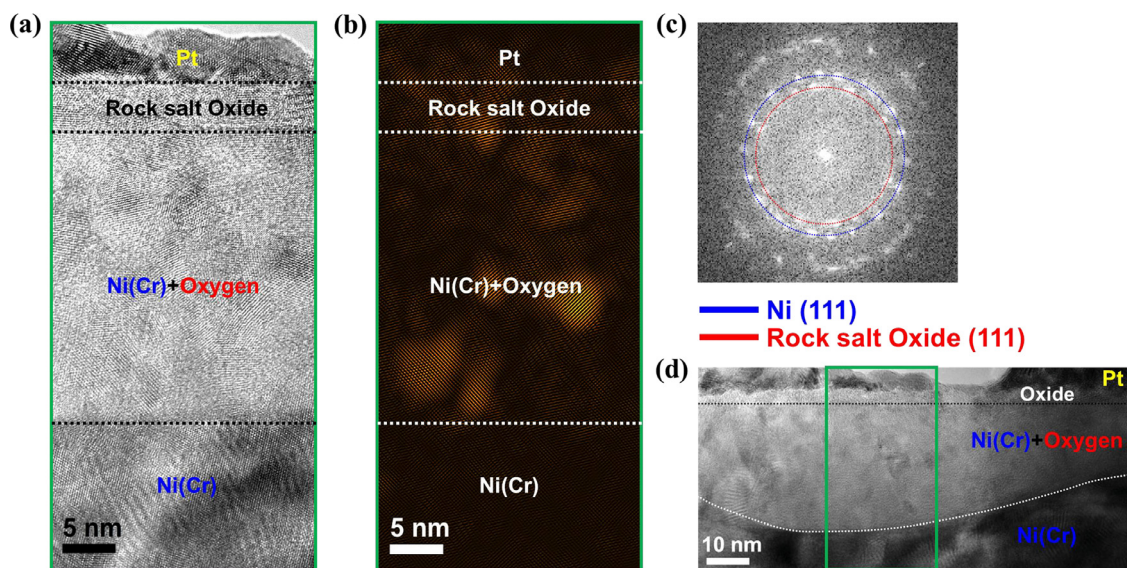


Fig. 2. TEM cross-section sample of NiCr after fast passivation (a) HREM image shows top rock salt layer and beneath rock salt and metal nanocrystalline. (b) Fourier filtered image highlights the rock salt distribution. (c) Power spectrum shows a rock salt-metal mixture. (d) Low magnification bright-field image of the cross-section sample, the imaging region of Fig. 2(a) is labeled in the green rectangle.

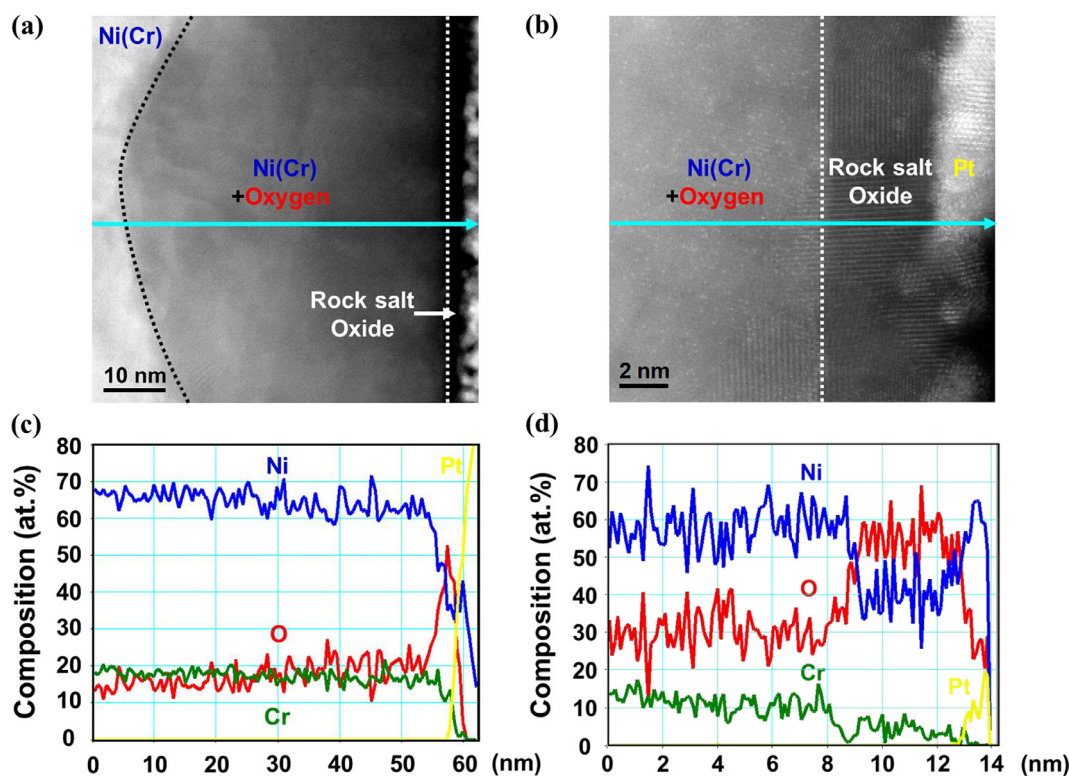


Fig. 3. NiCr fast passivation sample (a) ADF image of top oxide layer, oxygen injection region, and metal substrate. The interfaces between the three distinguished regions are labeled in dashed lines. (b) ADF image of top rock salt structure. (c) EDS composition profile shows a high concentration of O in the fcc Ni(Cr). (d) EDS profile shows Cr cations are captured in the rock salt oxide.

oxygen penetration and the oxide nucleation. The EDS compositional profile in Fig. 3 shows a high concentration of Cr in both the oxygen penetrating layers (Fig. 3(a) and (c)), and top rock salt oxide (Fig. 3(b) and (d)), due to nonequilibrium solute capture [41,45,47].

For the slow passivated NiCr sample, an oxygen penetration region is also observed under the rock salt top layer; see Fig. 4(a) and (b). However, the oxygen and Ni(Cr) mixture layer becomes localized rather than continuous with fewer rock salt nanocrystallites in the Ni(Cr)-O solid solution compared to the fast growth sample. Solute oxygen atoms introduce lattice distortions indicated by the slight orientation changes in Fig. 4(c), while the dominant structure remains fcc. The EDS compositional profile in Fig. 5(a) and (b) shows that the oxygen concentration decreases from the outer oxide surface towards the inner metal substrate, consistent with a diffusion process.

The oxygen penetration only occurred locally in the fast passivated NiCrMo sample in Fig. 6(a), comparable to the slow passivated NiCr case, except with an fcc Ni(Cr, Mo)-O solid solution. The oxygen introduced lattice distortion contributes to the diffraction contrast in the bright-field image, Fig. 6(a), and the phase contrast in the high-resolution image, Fig. 6(c). The compositional changes due to oxygen contribute to the atomic number or Z contrast in the dark-field image in Fig. 7(a). Both structural and chemical changes make the oxygen injection region distinguishable from the passive oxide above and the metal below. A high concentration of oxygen in the fcc Ni(Cr, Mo) lattice is also evidenced by the EDS compositional profile in Fig. 7.

The most important difference compared to the NiCr sample is that the top oxide layer is a corundum structure in Fig. 6(b). As we have seen in in-situ high-temperature gaseous oxidation experiments [47], the Mo addition promotes the nucleation rate of the corundum phase, which is consistent with the observation in the current aqueous corrosion case. The corundum oxide mitigates the

inward oxygen transport, evidenced by the distribution of rock salt particles concentrating in the upper part of the penetration region and far away from the metal/oxide interface in Fig. 6(c) and (d).

For the slow passivated NiCrMo sample, the nucleation of rock salt nanoparticles is even less, and the location is further from the metal beneath, as shown in Fig. 8. The top flat oxide layer has a corundum structure, and notably, the composition contains about 20 at.% ~30 at.% Ni by EDS line scanning in Fig. 9. The result shows that not only Cr can be captured in rock salt, but also Ni can be captured in corundum [41,45,47]. The formation of a metastable $\text{Ni}_{2-x}\text{Cr}_x\text{O}_3$ phase is a consequence of nonequilibrium solute capture [41], which is general during aqueous corrosion where interface velocities are large, particular in a fast growth rate such as repassivation.

4. Discussion

The experimental results indicate a significant difference in the altered layer of metal just under the oxide due to oxygen *inside* the metal, which is unexpected based upon established models where the metal is assumed to be somewhat passive (except for consequences of metal vacancies). As we will show, the reason for this is oxygen interstitial injection into the metal due to the high concentration of cation and metal vacancies.

4.1. Point defect flux

We will first establish the basics of the point defects using standard methods. According to the point defect model (PDM) [1,15,18], the typical defect reactions at the metal/oxide interface include (1) creation of metal vacancies, (2) generation of cation interstitials in the oxide, and (3) creation of oxygen vacancies. Here, we do not consider cation interstitials, which are not the dominant defects in

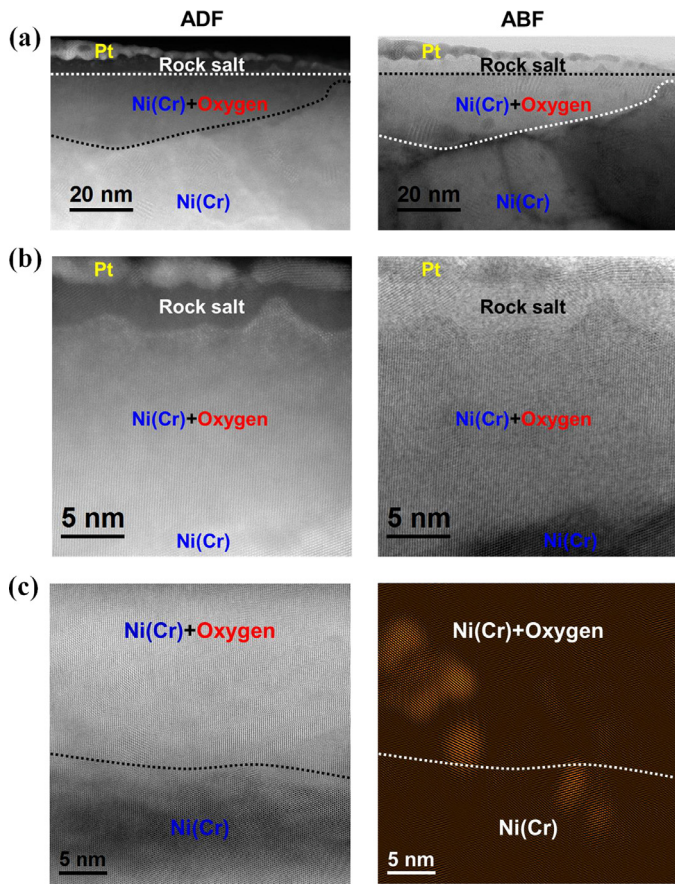


Fig. 4. TEM cross-section sample of NiCr after slow passivation (a) ADF and ABF images show localized oxygen penetrating region beneath flat rock salt layer. (b) ADF and ABF images of oxygen penetrating area with a higher magnification indicate a distorted metallic lattice. (c) HREM image and Fourier filtered image highlight rock salt distribution.

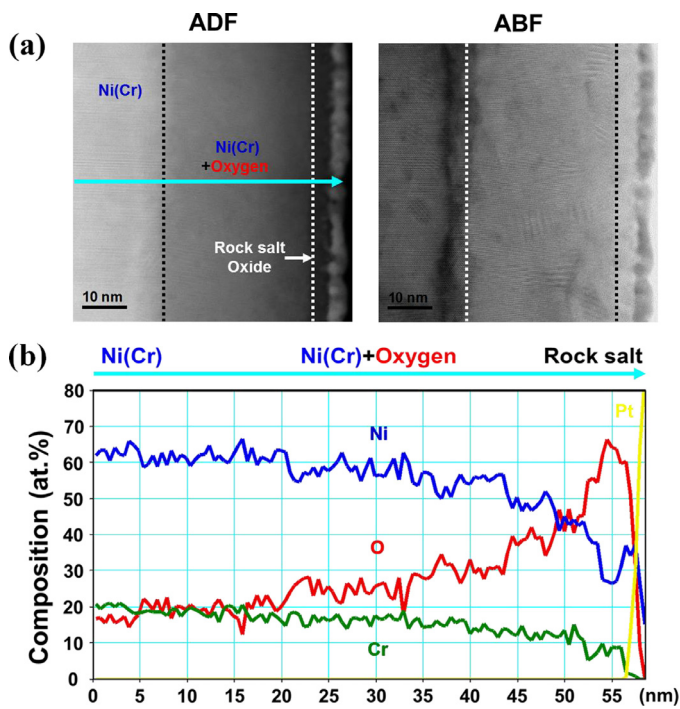


Fig. 5. NiCr slow passivation sample (a) ADF and ABF images of the layered oxidized region (b) EDS composition profile from the metal substrate to oxide surface.

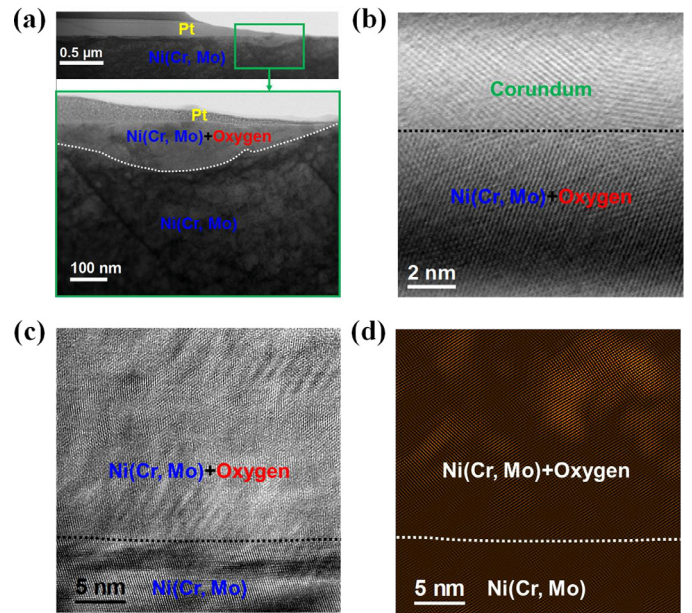


Fig. 6. NiCrMo fast passivation sample (a) Bright-field image shows localized oxygen penetrating region beneath top oxide layer (b) ABF image shows the top flat oxide is corundum structure. (c) HREM image shows the oxygen penetration region and metal. (d) Fourier filtered image highlights the rock salt distribution.

the rock salt structure [63,64] nor in corundum [65–67]. For simplicity, we will assume that the growth rate of oxide is much faster than the dissolution rate in the solution, as Fig. 1 supports. Therefore, the approximations and analysis in Generation I PDM [21] are appropriate.

The relationship between the working electrode and reference electrode in an electrochemical cell and the corresponding potentials are given by

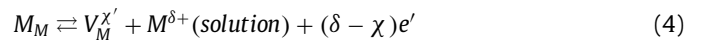
$$\phi_{M/O} + \phi_O + \phi_{O/S} = \phi_R + V \quad (1)$$

The parameters $\phi_{M/O}$, ϕ_O , $\phi_{O/S}$, ϕ_R represent the potential drops at the metal/oxide, across the oxide, oxide/solution, and solution/reference electrode interfaces, respectively. V is the applied potential.

Two reactions occur at the metal/oxide interface:



and at the oxide/solution interface:



where m represents the metal atom, M_M is the cation in oxide, v_m is the metal vacancy, $V_O^{\cdot\cdot}$ is the oxygen vacancy in oxide, $V_M^{\chi'}$ is a cation vacancy in the oxide with the charge of χ , and e' is an electron, $M^{\delta+}$ is the hydrated metal cation with the charge of δ in the electrolyte.

Specifically, (4) and (2) describe the generation of cation vacancies at the oxide/solution interface and the annihilation of cation vacancies at the metal/oxide interface. Similarly, (3) and (5) describe the generation and annihilation of oxygen vacancies, respectively.

For the (nonequilibrium) rock salt structure of $Ni_{1-x}Cr_xO$, the dominant transport mechanism is cation diffusion [63,64]. The

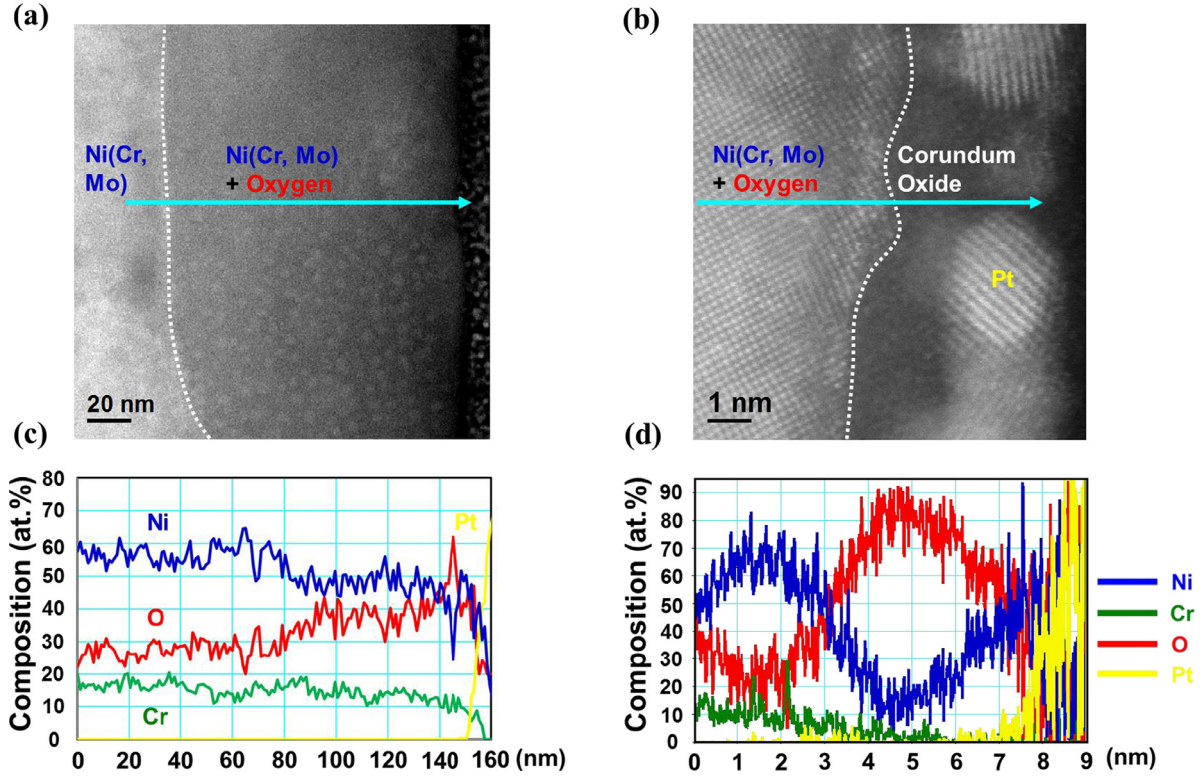


Fig. 7. NiCrMo fast passivation sample (a) ADF image of oxygen injection region and metal substrate. (b) ADF image of top corundum structure. (c) EDS composition profile shows a high concentration of O in the fcc Ni(Cr, Mo). (d) EDS profile shows Ni cations are captured in the corundum oxide.

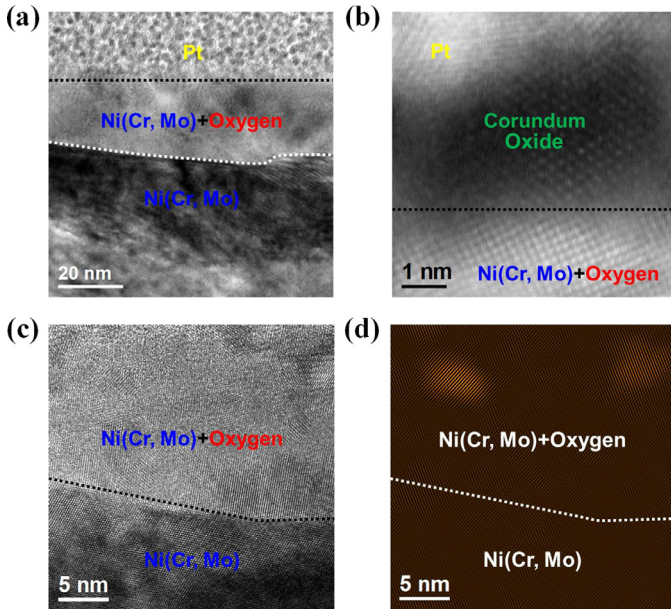


Fig. 8. TEM cross-section sample of NiCrMo after slow passivation (a) Bright field image (b) ADF image of top corundum structure. (c) HREM image shows the oxygen penetration region and metal. (d) Fourier filtered image highlights the rock salt distribution.

growth rate of the passive film is related to the flux of the cation vacancies,

$$\frac{dL}{dt} = \frac{\Omega}{N_V} J_{V_M^{X'}} \quad (6)$$

Where L is the thickness of oxide, t is time, dL/dt is the film growth rate, and $J_{V_M^{X'}}$ is the flux of $V_M^{X'}$, which can be calculated from the

Nernst–Planck equation:

$$J_{V_M^{X'}} = -D_{V_M^{X'}}^* \frac{\partial C_{V_M^{X'}}}{\partial x} - D_{V_M^{X'}}^* \frac{C_{V_M^{X'}}}{RT} \chi F \frac{\partial \phi}{\partial x} \quad (7)$$

$D_{V_M^{X'}}^*$ is the diffusivity of $V_M^{X'}$, F is Faraday constant. Assuming the electric field across the oxide film is independent of thickness so that

$$-\frac{\partial \phi}{\partial x} = \frac{\phi_0}{L} \quad (8)$$

$$\frac{\partial C_{V_M^{X'}}}{\partial x} = -\frac{J_{V_M^{X'}}}{D_{V_M^{X'}}^*} + \frac{C_{V_M^{X'}}}{RT} \chi F \frac{\phi_0}{L} \quad (9)$$

The integration of (9) along the cation diffusion path from the oxide/solution interface to the metal/oxide interface gives the flux of cation vacancies:

$$V_{M(M/O)}^{X'} \int_0^L \frac{dC_{V_M^{X'}}}{V_{M(O/S)}^{X'} \frac{\chi F \phi_0}{RT} C_{V_M^{X'}} - \frac{J_{V_M^{X'}}}{D_{V_M^{X'}}^*}} = \int_0^L dx \quad (10)$$

$$J_{V_M^{X'}} = \chi K D_{V_M^{X'}}^* \frac{\exp(\chi KL) C_{V_M^{X'}(O/S)} - C_{V_M^{X'}(M/O)}}{\exp(\chi KL) - 1} \quad (11)$$

where $K = \frac{F \phi_0}{RT}$. Under galvanostatic conditions dominated by oxide growth as opposed to cation ejection, the electrochemical current density is:

$$i = 2F \frac{N_V}{\Omega} \frac{dL}{dt} = \text{Constant} \quad (12)$$

Combining Eq. (6)–(12),

$$C_{V_M^{X'}(O/S)} = \frac{RT}{4F^2 D_{V_M^{X'}}^* E} i \quad (13)$$

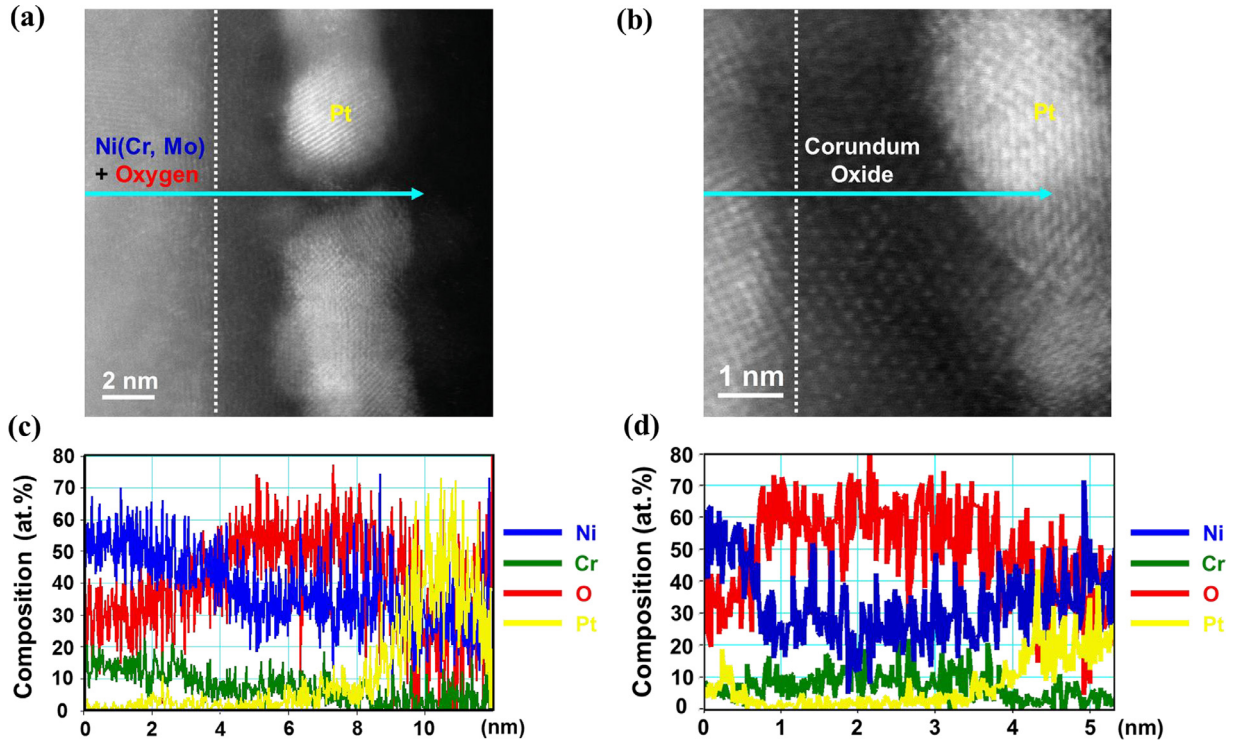


Fig. 9. NiCrMo after slow passivation (a) ADF image of oxygen injection region and top oxide layer. (b) ADF image of top corundum structure. (c) EDS line profile shows O in the Ni(Cr, Mo). (d) EDS profile of the top corundum layer shows the solute capture of Ni.

where $E = \phi_0/L$ is the electric field strength across oxide.

From Eq. (13), the cation vacancies $C_{V_M^{X'}(O/S)}$ generated at the oxide/solution interface is proportional to the current i and inversely proportional to the electric field strength E and electrochemical diffusivity of $V_M^{X'}$ through the oxide film.

Similarly, for the corundum structure of Cr_2O_3 , the dominant transport mechanism is the inward oxygen diffusion at room temperature and ambient oxygen pressure [68]. The concentration of oxygen vacancies created at the metal/oxide interface as a function of current density:

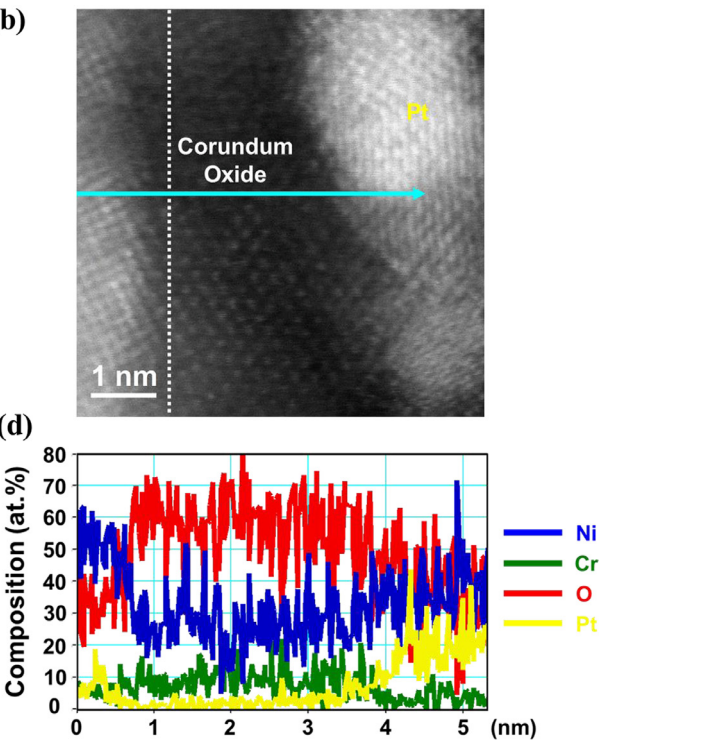
$$C_{V_O(M/O)} = \frac{RT}{4F^2 D_{V_O}^* E} i \quad (14)$$

$D_{V_O}^*$ is the diffusivity of $V_O^{\bullet\bullet}$.

To verify Eq. (13), we use the experimental parameters to estimate the cation vacancies near the oxide surface. From the EDS profile in Fig. 3(b), there are 55 at. % O, 40 at. % Ni, and 5 at. % Cr. The 5 at. % Cr is a charge equivalence of 7.5 at. % Ni given the differences in oxidation state and charge neutral, thus the composition is equivalent to 55 at. % O and 47.5 at. % Ni. Normalizing the composition and according to the stoichiometry of NiO, there are about 6.8 at. % Ni vacancies in the rock salt layer.

Taking the temperature as 298.15 K, the galvanostatic current density as $50 \mu\text{A}/\text{cm}^2$ in the fast growth of NiCr sample, $D_{V_M^{X'}}^*$ of Ni vacancies in the rock salt is in the order of $1.0 \times 10^{-18} \text{ m}^2/\text{s}$, and the electric field E across is of the order of 1 V/nm, Eq. (13) yields a cation vacancies concentration $C_{V_M^{X'}(O/S)}$ of about $33.3 \text{ mol}/\text{m}^3$.

Considering that the molar mass and density of NiO are 74.7 g/mol and $6.67 \text{ g}/\text{cm}^3$, the inverse of the molar volume of rock salt is $892.9 \text{ mol}/\text{m}^3$. Hence the fraction of cation vacancies in rock salt is about 3.7 at. %, which is in the same order of magnitude as 6.8 at. % in the experiments, although the exact value depends on the more accurate data regarding $D_{V_M^{X'}}^*$ and E .



From the analysis above, a large current density produces a high concentration of defects. For the cation diffusion dominated rock salt, cation vacancies are generated at the oxide/solution interface and then transport towards the metal/oxide interface. For the oxygen diffusion dominated corundum, oxygen vacancies are generated at the metal/oxide interface and then diffuse through the oxide film and annihilate on the oxide surface.

4.2. Oxygen injection

From the conventional analysis in the prior section, there will be a high concentration of cation vacancies in the rock salt and oxygen vacancies in the corundum structure. We now show that this naturally leads to the injection of oxygen interstitials into metal for the rock salt case, as observed experimentally. What needs to be included is that the metal can act as a sink/source of electrons.

For a cation diffusion dominated oxide, such as rock salt, with significant cation vacancies in the oxide, consider the following reaction:



where O_i is an oxygen interstitial in the metal. Equating the electrochemical potentials on both sides:

$$\mu_{V_M^{X'}} + \chi F \phi_{\text{Oxide}} = \mu_{O_i} + \chi \mu_e + \chi F \phi_{\text{Metal}} \quad (16)$$

The change in Gibb's energy for reaction (15) is given by

$$\Delta G = \mu_{O_i}^\circ + \chi \mu_e^\circ + \chi F \phi_{M/O} - \mu_{V_M^{X'}}^\circ - RT \ln \left[\frac{\Omega}{N_V} \frac{C_{V_M^{X'}(M/O)}}{C_{O_i(M/O)}} \right] \quad (17)$$

where ϕ_{Oxide} and ϕ_{Metal} are flatband potentials for the oxide and metal, μ° is the standard chemical potential of species. This indicates that a high concentration of cation vacancies in the rock salt oxide drives oxygen interstitials into the metal, particularly as the metal acts as a sink for electrons.

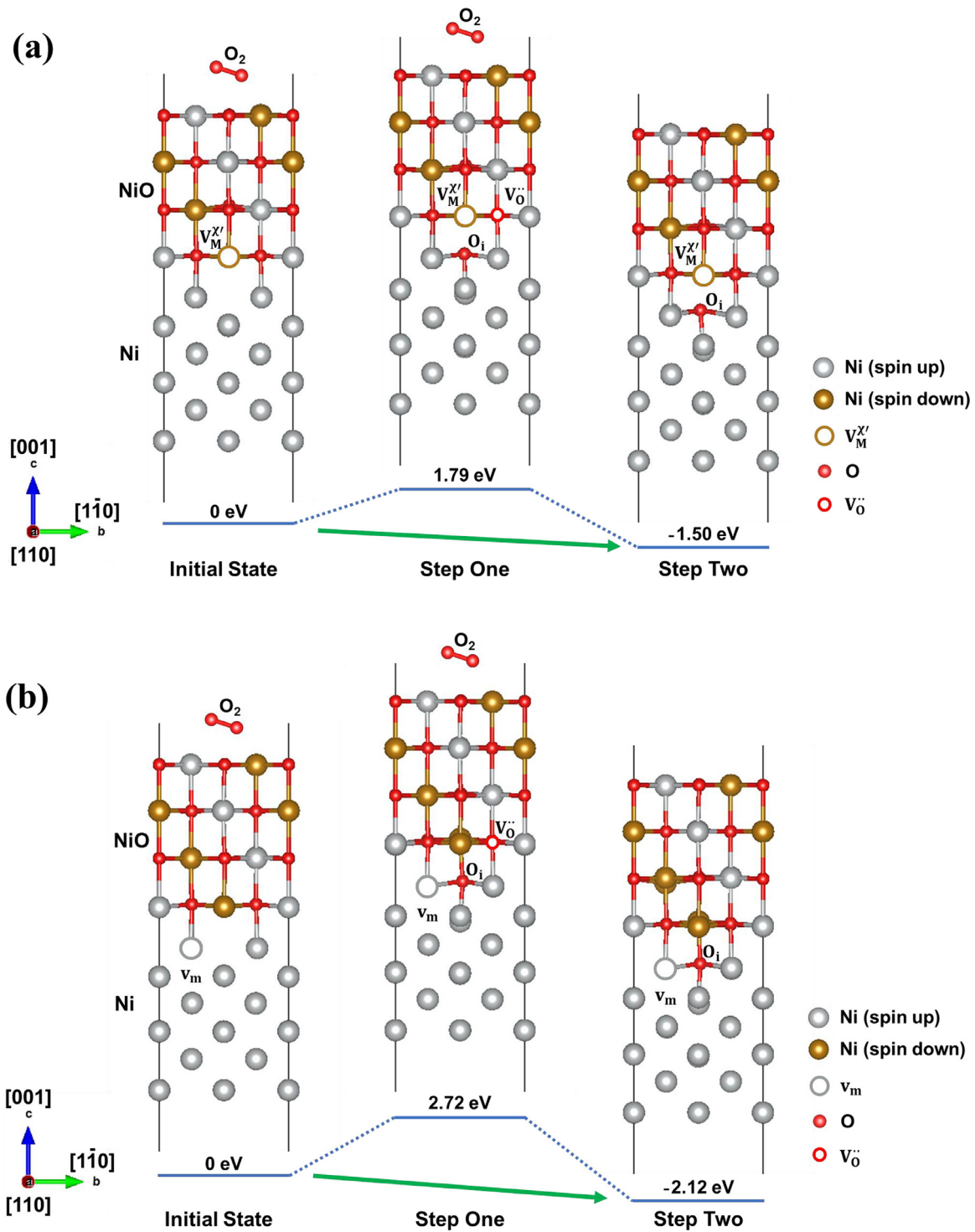


Fig. 10. The energy changes in the formation of oxygen interstitial with (a) cation vacancy and (b) metal vacancy at the Ni/NiO interface.

In contrast, for an anion diffusion dominated oxide, such as corundum,



Equating the electrochemical potentials on both sides:

$$\mu_{O_o} + 2F\phi_{Oxide} = \mu_{V_O^{..}} + \mu_{O_i} + 2\mu_{e'} + 2F\phi_{Metal} \quad (19)$$

The change in Gibb's energy for reaction (19) is given by

$$\Delta G = \mu_{V_O^{..}}^{\circ} + \mu_{O_i}^{\circ} + 2\mu_{e'}^{\circ} + 2F\phi_{M/O} - \mu_{O_o}^{\circ} + RT \ln \left[\frac{\Omega}{N_V} C_{V_O^{..}(M/O)} C_{O_i(M/O)} \right] \quad (20)$$

Now the opposite occurs; oxygen vacancies in a corundum oxide reduce oxygen interstitials' concentration in the alloy.

To validate the hypothesis on reaction 15, we calculated the energy change employing a NiO/Ni slab model using density functional theory, as shown in Fig. 10. As a benchmark, the lattice constant, formation energy, bandgap, and magnetic moment of Ni and Cr atoms in NiO and Cr₂O₃ are shown in Table 1. (As mentioned earlier, the bandgap and magnetic moments in the oxide are too small, a compromise to adequately represent the metals.)

Table 1

Lattice constants, bandgap, and magnetic moment of Ni and Cr atoms in NiO and Cr₂O₃, using the SCAN functional.

Parameters	NiO		Cr ₂ O ₃	
	This work	Experiment	This work	Experiment
a (Å)	4.15	4.18 [69]	4.95	4.95 [70]
c (Å)			13.62	13.57 [70]
c/a			2.75	2.74 [70]
Formation energy (eV/atom)	-1.39	-1.24*	-2.63	-2.34*
Band gap (eV)	2.39	4.3 [71]	2.81	3.4 [72]
Magnetic moment (μ _B)	1.56	1.77 [73]	2.77	3.8 [70]

* Standard enthalpy of formation at 25°C and 1 atmosphere of pressure.

Table 2

The energy changes in the formation of oxygen interstitial with and without cation and metal vacancies at the oxide/metal interface.

Energy (eV)	NiO/Ni Slab Model	
Oxygen interstitial	Step One	Step Two
Without vacancy	2.16	-1.71
With cation vacancy	1.79	-1.50
With metal vacancy	2.72	-2.12

Two reaction steps are considered; step one is the formation of oxygen interstitial in the metal, leaving an oxygen vacancy in the oxide; step two is the annihilation of oxygen vacancy. We compare the energy changes with and without cation and metal vacancies at the oxide/metal interface, as shown in Fig. 10.

From the results in Fig. 10 and Table 2, it can be seen that oxygen needs to overcome an energy barrier of 2.16 eV to create an oxygen vacancy in the oxide and jump from the oxide into the metal in step one. However, the overall energy decreases by 1.71 eV after the annihilation of oxygen vacancies on the oxide surface during step two. Moreover, the presence of cation vacancies decreases the energy barrier (step one) to 1.79 eV for the formation of an oxygen vacancy in the oxide and interstitial oxygen in the metal. The metal vacancy at the oxide/metal interface decreases the free energy by 2.12 eV after the oxygen vacancies are filled (step two). We note that the absolute energy changes calculated in the NiO and Ni bulk models are different from the NiO/Ni slab models, but the major conclusions still hold. Within the limits of the calculations, the results support the analytical analysis.

4.3. Creation of mixed metal/oxide region

From the above analysis, both analytical and via density functional theory, cation vacancies near the interface promote the injection of oxygen interstitials into the alloy. The solubility of oxygen in nickel in equilibrium with NiO is only 0.0175 at. % at 800°C [52] and the levels detected in the experiments are far above this. At slow growth rates, a high solubility regime is evident; at high growth rates, the experimental evidence indicates that rock salt oxides are precipitating inside the metal. Since the fast growth rate leads to more breakdown events, it is logical to connect the oxide precipitation to the breakdown directly; a mixed alloy/oxide phase will have significantly more local strain, defects, and higher-energy interfaces, so it can be expected to not provide as much corrosion resistance.

4.4. The role of Mo

The addition of Mo promotes the formation of corundum in the outer oxide layer for the NiCrMo alloy. This was shown in Figs. 6–9. This difference in oxide changes the transport mechanism as well as the diffusivity of oxygen through the oxide film and across the metal/oxide interface. As discussed above, an anion diffusion dominated oxide such as corundum alleviates the oxygen injection com-

pared to rock salt oxide, in which the dominated cation vacancies facilitate the oxygen transport into the metal.

5. Conclusions

The fast and slow corrosion of NiCr and NiCrMo was performed by galvanostat experiments in 0.1 M NaCl (pH 4) deaerated solution. Oxygen solid-solution regions were found beneath the outer oxides throughout TEM cross-sectioning, and the supersaturated oxygen atoms distorted the fcc metallic lattices. Oxygen injection into metal is more significant at a fast growth rate brought by a large passivation current density for the NiCr alloy, where there is a high volume of rock salt nanocrystals mixed with the Ni(Cr)-O solid solution. The faster growth leads to greater susceptibility to Cl⁻ induced breakdown, consistent with the potentiostatic experiments following. Mo addition promotes the corundum formation in the external oxide layer for NiCrMo, which changes the transport mechanism as well as the diffusivity of oxygen through the oxide film and across the metal/oxide interface. Consequently, only localized oxygen penetration is observed in this case. The corundum is more protective.

Declaration of Competing Interest

The authors declare that they have no known competing financial interests or personal relationships that could have appeared to influence the work reported in this paper.

Acknowledgments

This work was supported by ONR MURI “Understanding Atomic Scale Structure in Four Dimensions to Design and Control Corrosion Resistant Alloys” on Grant Number N00014-16-1-2280. We thank Dr. Penghao Xiao at Lawrence Livermore National Laboratory for beneficial discussions.

References

- [1] D.D. Macdonald, Passivity—the key to our metals-based civilization, *Pure Appl. Chem.* 71 (6) (1999) 951–978.
- [2] C. Wagner, Beitrag zur theorie des anlaufvorgangs, *Zeitschrift für physikalische Chemie* 21 (1) (1933) 25–41.
- [3] N. Mott, The theory of the formation of protective oxide films on metals, II, *Trans. Faraday Soc.* 35 (1940) 472–483.
- [4] N. Mott, The theory of the formation of protective oxide films on metals.—III., *Trans. Faraday Soc.* 43 (1947) 429–434.
- [5] N. Cabrera, N.F. Mott, Theory of the oxidation of metals, *Rep. Prog. Phys.* 12 (1948) 163–184.
- [6] M. Bojinov, G. Fabricius, T. Laitinen, K. Mäkelä, T. Saario, G. Sundholm, Coupling between ionic defect structure and electronic conduction in passive films on iron, chromium and iron–chromium alloys, *Electrochim. Acta* 45 (13) (2000) 2029–2048.
- [7] C. Chainais-Hillairet, C. Bataillon, Mathematical and numerical study of a corrosion model, *Numer. Math.* 110 (1) (2008) 1–25.
- [8] C. Bataillon, F. Bouchon, C. Chainais-Hillairet, C. Desgranges, E. Hoarau, F. Martin, S. Perrin, M. Tupin, J. Talandier, Corrosion modelling of iron based alloy in nuclear waste repository, *Electrochim. Acta* 55 (15) (2010) 4451–4467.
- [9] K. Leistner, C. Toulemonde, B. Diawara, A. Seyeux, P. Marcus, Oxide film growth kinetics on metals and alloys II. Numerical simulation of transient behavior, *J. Electrochem. Soc.* 160 (6) (2013) C197–C205.
- [10] A. Seyeux, V. Maurice, P. Marcus, Oxide film growth kinetics on metals and alloys I. Physical model, *J. Electrochem. Soc.* 160 (6) (2013) C189–C196.
- [11] A. Couet, A.T. Motta, A. Ambard, The coupled current charge compensation model for zirconium alloy fuel cladding oxidation: I. Parabolic oxidation of zirconium alloys, *Corros. Sci.* 100 (2015) 73–84.
- [12] M. Momeni, J.C. Wren, A mechanistic model for oxide growth and dissolution during corrosion of Cr-containing alloys, *Faraday Discuss* 180 (2015) 113–135.
- [13] Q.C. Sherman, P.W. Voorhees, Phase-field model of oxidation: Equilibrium, *Phys. Rev. E* 95 (3–1) (2017) 032801.
- [14] R. Ramanathan, P.W. Voorhees, Morphological stability of steady-state passive oxide films, *Electrochim. Acta* 303 (2019) 299–315.
- [15] C. Chao, L. Lin, D. Macdonald, A point defect model for anodic passive films: I. Film growth kinetics, *J. Electrochem. Soc.* 128 (6) (1981) 1187.
- [16] L. Lin, C. Chao, D. Macdonald, A point defect model for anodic passive films II. Chemical breakdown and pit initiation, *J. Electrochem. Soc.* 128 (6) (1981) 1194–1198.

- [17] C. Chao, L. Lin, D. Macdonald, A point defect model for anodic passive films III. Impedance response, *J. Electrochem. Soc.* 129 (9) (1982) 1874–1879.
- [18] D.D. Macdonald, The point defect model for the passive state, *J. Electrochem. Soc.* 139 (12) (1992) 3434.
- [19] J. Jin Kim, S. Hun Shin, J. Ang Jung, K. Joon Choi, J. Hyun Kim, First-principles study of interstitial diffusion of oxygen in nickel chromium binary alloy, *Appl. Phys. Lett.* 100 (13) (2012) 131904.
- [20] V. Alexandrov, M.L. Sushko, D.K. Schreiber, S.M. Brummer, K.M. Rosso, Ab initio modeling of bulk and intragranular diffusion in Ni alloys, *J. Phys. Chem. Lett.* 6 (9) (2015) 1618–1623.
- [21] D.D. Macdonald, The history of the point defect model for the passive state: a brief review of film growth aspects, *Electrochim. Acta* 56 (4) (2011) 1761–1772.
- [22] X.-xX. Yu, L.D. Marks, Combining the physics of metal/oxide heterostructure, interface dipole, band bending, crystallography, and surface state to understand heterogeneity contrast in oxidation and corrosion, *Corrosion* 75 (2) (2019) 152–166.
- [23] D. Douglass, The oxidation mechanism of dilute Ni-Cr alloys, *Corros. Sci.* 8 (9) (1968) 665–678.
- [24] R. Hales, A. Hill, The role of metal lattice vacancies in the high-temperature oxidation of nickel, *Corros. Sci.* 12 (11) (1972) 843–853.
- [25] G. Gibbs, R. Hales, The influence of metal lattice vacancies on the oxidation of high temperature materials, *Corros. Sci.* 17 (6) (1977) 487–507.
- [26] Y. Shida, G. Wood, F. Stott, D. Whittle, B. Bastow, Intergranular oxidation and internal void formation in Ni-40% Cr alloys, *Corros. Sci.* 21 (8) (1981) 581–597.
- [27] H. Evans, Cavity formation and metallurgical changes induced by growth of oxide scale, *Mater. Sci. Technol.* 4 (12) (1988) 1089–1098.
- [28] D.J. Young, *High Temperature Oxidation and Corrosion of Metals*, Elsevier, 2008.
- [29] C. Desgranges, F. Lequien, E. Aublant, M. Nastar, D. Monceau, Depletion and voids formation in the substrate during high temperature oxidation of Ni-Cr alloys, *Oxid. Met.* 79 (1–2) (2013) 93–105.
- [30] H.-H. Strehblow, P. Marcus, Mechanisms of pitting corrosion, *Corros. Mech. Theory Pract.* (1995) 201–238.
- [31] P.I. Marshall, G.T. Burstein, Effects of alloyed molybdenum on the kinetics of repassivation on austenitic stainless steels, *Corros. Sci.* 24 (5) (1984) 463–478.
- [32] R.S. Lillard, M.P. Jurinski, J.R. Scully, Crevice corrosion of alloy 625 in chlorinated ASTM artificial ocean water, *Corrosion* 50 (4) (1994) 251–265.
- [33] A. Lloydys, J. Noël, D. Shoesmith, N. McIntyre, The open-circuit ennoblement of alloy C-22 and other Ni-Cr-Mo alloys, *JOM* 57 (1) (2005) 31–35.
- [34] N. Ebrahimi, P. Jakupi, J. Noel, D. Shoesmith, The role of alloying elements on the crevice corrosion behavior of Ni-Cr-Mo alloys, *Corrosion* 71 (12) (2015) 1441–1451.
- [35] M. Urquidi, D.D. Macdonald, Solute-vacancy interaction model and the effect of minor alloying elements on the initiation of pitting corrosion, *J. Electrochem. Soc.* 132 (3) (1985) 555.
- [36] A.C. Lloyd, J.J. Noël, S. McIntyre, D.W. Shoesmith, Cr, Mo and W alloying additions in Ni and their effect on passivity, *Electrochim. Acta* 49 (17–18) (2004) 3015–3027.
- [37] N. Ebrahimi, M. Biesinger, D. Shoesmith, J. Noël, The influence of chromium and molybdenum on the repassivation of nickel-chromium-molybdenum alloys in saline solutions, *Surf. Interface Anal.* 49 (13) (2017) 1359–1365.
- [38] C. Clayton, Y. Lu, A bipolar model of the passivity of stainless steel: the role of Mo addition, *J. Electrochem. Soc.* 133 (12) (1986) 2465–2473.
- [39] B. Kehler, G. Ilevbare, J. Scully, Crevice corrosion stabilization and repassivation behavior of alloy 625 and alloy 22, *Corrosion* 57 (12) (2001) 1042–1065.
- [40] E.B. Haugan, M. Næss, C.T. Rodriguez, R. Johnsen, M. Iannuzzi, Effect of tungsten on the pitting and crevice corrosion resistance of Type 25Cr super duplex stainless steels, *Corrosion* 73 (1) (2017) 53–67.
- [41] X.-xx. Yu, A. Gulec, Q. Sherman, K.L. Cwalina, J.R. Scully, J.H. Perepezko, P.W. Voorhees, L.D. Marks, Nonequilibrium solute capture in passivating oxide films, *Phys. Rev. Lett.* 121 (14) (2018) 145701.
- [42] R. Ramanathan, P.W. Voorhees, Departures from local interfacial equilibrium during metal oxidation, *Phys. Rev. Mater.* 4 (11) (2020) 113401.
- [43] A. Takei, K. Nii, Growth process of oxide layers in the initial stage of oxidation of 80 Ni-20 Cr alloy, *Jpn. Inst. Metals* 36 (9) (1972) 853–859.
- [44] X.X. Yu, A. Gulec, A. Yoon, J.M. Zuo, P.W. Voorhees, L.D. Marks, Direct observation of “Pac-Man” coarsening, *Nano Lett.* 17 (8) (2017) 4661–4664.
- [45] X.-xX. Yu, A. Gulec, K.L. Cwalina, J.R. Scully, L.D. Marks, New insights on the role of chloride during the onset of local corrosion: TEM, APT, surface energy, and morphological instability, *Corrosion* 75 (6) (2019) 616–627.
- [46] X.-X. Yu, J.H. Perepezko, L.D. Marks, Crystallographic anisotropy of nonequilibrium solute capture, *Acta Mater.* (2020).
- [47] X.-xX. Yu, A. Gulec, C.M. Andolina, E.J. Zeitchick, K. Gusieva, J.C. Yang, J.R. Scully, J.H. Perepezko, L.D. Marks, In situ observations of early stage oxidation of Ni-Cr and Ni-Cr-Mo alloys, *Corrosion* 74 (9) (2018) 939–946.
- [48] K.L. Cwalina, C. Demarest, A. Gerard, J. Scully, Revisiting the effects of molybdenum and tungsten alloying on corrosion behavior of nickel-chromium alloys in aqueous corrosion, *Curr. Opin. Solid State Mater. Sci.* (2019).
- [49] R.P. Elliott, *Constitution of Binary Alloys*, McGraw-Hill, New York, 1965.
- [50] R. Wasilewski, The solubility of oxygen in, and the oxides of, tantalum, *J. Am. Chem. Soc.* 75 (4) (1953) 1001–1002.
- [51] A. Seybolt, Solid solubility of oxygen in columbium, *Jom* 6 (6) (1954) 774–776.
- [52] J.-W. Park, C.J. Altstetter, The diffusion and solubility of oxygen in solid nickel, *Metall. Trans. A* 18 (1) (1987) 43–50.
- [53] G. Kresse, J. Hafner, Ab initio molecular dynamics for liquid metals, *Phys. Rev. B* 47 (1) (1993) 558–561.
- [54] G. Kresse, J. Furthmüller, Efficient iterative schemes for ab initio total-energy calculations using a plane-wave basis set, *Phys. Rev. B* 54 (16) (1996) 11169–11186.
- [55] G. Kresse, D. Joubert, From ultrasoft pseudopotentials to the projector augmented-wave method, *Phys. Rev. B* 59 (3) (1999) 1758–1775.
- [56] P.E. Blochl, Projector augmented-wave method, *Phys. Rev. B Condens. Matter* 50 (24) (1994) 17953–17979.
- [57] J. Sun, A. Ruzsinszky, J.P. Perdew, Strongly constrained and appropriately normed semilocal density functional, *Phys. Rev. Lett.* 115 (3) (2015) 036402.
- [58] J. Sun, R.C. Remsing, Y. Zhang, Z. Sun, A. Ruzsinszky, H. Peng, Z. Yang, A. Paul, U. Waghmare, X. Wu, Accurate first-principles structures and energies of diversely bonded systems from an efficient density functional, *Nat. Chem.* 8 (9) (2016) 831.
- [59] H.J. Monkhorst, J.D. Pack, Special points for brillouin-zone integrations, *Phys. Rev. B* 13 (12) (1976) 5188–5192.
- [60] K. Ogle, Atomic emission spectroelectrochemistry: real-time rate measurements of dissolution, corrosion, and passivation, *Corrosion* 75 (12) (2019) 1398–1419.
- [61] K. Lutton, K. Gusieva, N. Ott, N. Birbilis, J.R. Scully, Understanding multi-element alloy passivation in acidic solutions using operando methods, *Electrochem. Commun.* 80 (2017) 44–47.
- [62] K.L. Cwalina, H.M. Ha, N. Ott, P. Reinke, N. Birbilis, J.R. Scully, In operando analysis of passive film growth on Ni-Cr and Ni-Cr-Mo alloys in chloride solutions, *J. Electrochem. Soc.* 166 (11) (2019) C3241–C3253.
- [63] M. O’Keeffe, W.J. Moore, Diffusion of oxygen in single crystals of nickel oxide, *J. Phys. Chem.* 65 (8) (1961) 1438–1439.
- [64] A. Oxidation, R. Taylor, The self-diffusion of Ni in NiO and its relevance to the oxidation of Ni, *J. Mater. Sci.* 13 (2) (1978) 427–432.
- [65] X. Ledoux, S. Mathieu, M. Vilasi, Y. Wouters, P. Del-Gallo, M. Wagner, Oxide growth characterization during short-time oxidation of a commercially available chromia-forming alloy (HR-120) in air at 1,050 degrees C, *Oxid. Met.* 80 (1–2) (2013) 25–35.
- [66] A.C.S. Sabioni, E.A. Malheiros, V. Ji, F. Jomard, W.A.D. Macedo, P.L. Gastelois, Ion diffusion study in the oxide layers due to oxidation of AISI 439 ferritic stainless steel, *Oxid. Met.* 81 (3–4) (2014) 407–419.
- [67] S. Voyshnis, A. Seyeux, S. Zanna, B. Martin-Cabanas, T. Couvant, P. Marcus, Oxide layer growth on nickel-base alloy surfaces in high temperature water and in O₂ studied by ToF-SIMS with isotopic tracers, *Corros. Sci.* 145 (2018) 212–219.
- [68] C. Poulain, A. Seyeux, S. Voyshnis, P. Marcus, Volatilization and transport mechanisms during Cr oxidation at 300°C studied in situ by ToF-SIMS, *Oxid. Met.* 88 (3) (2017) 423–433.
- [69] S. Sasaki, K. Fujino, Y. Takéuchi, X-ray determination of electron-density distributions in oxides, MgO, MnO, CoO, and NiO, and atomic scattering factors of their constituent atoms, *Proc. Jpn. Acad., Ser. B* 55 (2) (1979) 43–48.
- [70] L.W. Finger, R.M. Hazen, Crystal structure and isothermal compression of Fe₂O₃, Cr₂O₃, and V₂O₃ to 50 kbars, *J. Appl. Phys.* 51 (10) (1980) 5362–5367.
- [71] G.A. Sawatzky, J.W. Allen, Magnitude and origin of the band-gap in NiO, *Phys. Rev. Lett.* 53 (24) (1984) 2339–2342.
- [72] J.A. Crawford, R.W. Vest, Electrical conductivity of single-crystal Cr₂O₃, *J. Appl. Phys.* 35 (8) (1964) 2413–2418.
- [73] A. Cheetham, D. Hope, Magnetic ordering and exchange effects in the antiferromagnetic solid solutions Mn x Ni 1– x O, *Phys. Rev. B* 27 (11) (1983) 6964.